

Article

Selective Hydrogenation of Naphthalene over γ -Al₂O₃-Supported NiCu and NiZn Bimetal Catalysts

Jingqiu Li ^{1,2,3}, Liu Shi ⁴, Gang Feng ⁴, Zhangping Shi ³ , Chenglin Sun ^{1,*} and Dejin Kong ³¹ Dalian Institute of Chemical Physics, Chinese Academy of Science, Dalian 116023, China; lijq.sshy@sinopec.com² University of Chinese Academy of Science, Beijing 100049, China³ State Key Laboratory of Green Chemical Engineering and Industrial Catalysis, Shanghai Research Institute of Petrochemical Technology, SINOPEC, Shanghai 201208, China; shizhp.sshy@sinopec.com (Z.S.); kongdj.sshy@sinopec.com (D.K.)⁴ Key Laboratory of Jiangxi Province for Environment and Energy Catalysis, Institute of Applied Chemistry, College of Chemistry, Nanchang University, No. 999 Xuefu Road, Nanchang 330031, China; shiliu@email.ncu.edu.cn (L.S.); fenggang@ncu.edu.cn (G.F.)

* Correspondence: clsun@dicp.ac.cn; Tel.: +86-411-8437-9133

Received: 28 August 2020; Accepted: 6 October 2020; Published: 20 October 2020



Abstract: A series of Cu and Zn modified Ni/Al₂O₃ catalysts were prepared using an incipient impregnation method for the selective hydrogenation of naphthalene into tetralin. X-ray diffraction (XRD), H₂-Temperature programmed reduction (H₂-TPR), transmission electron microscopy (TEM) and X-ray photoelectron spectroscopy (XPS) were applied to reveal the structure regulation, and density functional theory (DFT) calculations were performed to investigate the electronic effect and reactant adsorptions on the active sites. The results showed that the addition of CuO promoted the hydrogenation of naphthalene with an inhibited tetraline selectivity. However, a simultaneously increasing naphthalene conversion and tetraline selectivity were achieved over the Zn modified Ni/Al₂O₃ catalysts. The characterization and calculation results revealed that the doping of CuO improved the hydrogenation activity with a low tetralin selectivity due to the H spillover from the Cu. The addition of ZnO decreased the interaction between NiO_x and Al₂O₃ in NiZn/Al₂O₃ catalysts, which efficiently increased the reduction ability of NiO_x species and, thus, improved the naphthalene hydrogenation activity. The electron transfer from ZnO to NiO_x weakened the adsorption of tetraline and resulted in increased tetraline selectivity. This work provides insight into developing efficient catalysts for heavy aromatics conversions via rational surface engineering.

Keywords: heavy aromatics; tetraline; naphthalene; nickel-based catalysts; selective hydrogenation

1. Introduction

With the rapid expansion of oil refining, and the aromatics and ethylene industry, the production of heavy aromatics byproducts also increased dramatically, producing millions of tons of heavy aromatics in China [1]. The composition of these heavy aromatics is complicated, and typically contains the condensed ring compounds, which makes them not suitable for the direct blending of oil products or chemical utilization. Hence, it is urgent to develop new methods to utilize the large quantity of heavy aromatics. On the other hand, the light aromatics are an important category of basic chemical raw materials and additives for the high octane oils. The market demand of light aromatics, such as benzene, toluene, xylene (BTX), etc., is flourishing [2–7]. Hence, efficiently converting the heavy aromatics into light aromatics can realize the diversification of the raw materials for light aromatics producing, which is of significant economic value.

For the efficient catalytic conversion of heavy aromatics into BTX, the corresponding catalysts must possess appropriate hydrocracking activity [8–12]. Namely, in this process, the condensed ring compound should be precisely hydrogenated into mononuclear aromatics and then cracked into BTX. Hence, selective catalytic hydrogenation is the most important key technology in the catalyst design, which ensures the catalytic efficiency as well as the selectivity. Naphthalene is the simplest condensed ring aromatic, which is typically used as the probe molecule for the investigation of selective hydrocracking of heavy aromatics [4,13–15]. The selective hydrocracking process includes the hydrogenation of naphthalene into tetralin and the following cracking of tetralin into BTX. The deep hydrogenation of tetralin to decalin should be prevented [11,16].

Ni/Al₂O₃ catalysts used in the hydrogenation of naphthalene have been reported recently, and the studies were mainly focused on the preparation of catalysts and the operating conditions of the reaction [17–24]. The adsorption modes of naphthalene on the active sites of the Ni/Al₂O₃ were also investigated via theoretical calculations, such as the π and π/σ adsorption modes of the aromatic ring on the Ni surface as well as the σ desorption mode of tetralin from the Ni surface, which play important roles in the catalytic reactions [25]. However, the electronic structure adjustment of the Ni active sites and the resulting changes of the adsorption modes and selective hydrogenation activity are still rarely reported, making the mechanism and regulation rules for the selective hydrogenation of naphthalene over the Ni-based catalysts still unclear.

Herein, we introduced Cu and Zn as two typical electronic structure promoters to Ni/Al₂O₃ catalysts, and investigated their catalytic performances for naphthalene selective hydrogenation thoroughly. The influences of the above promoters on the structure and hydrogenation properties of Ni/Al₂O₃ catalysts were studied via the necessary characterizations, and the density functional theory (DFT) calculations were then performed to reveal the electron transfer effect between Ni and promoters as well as the adsorption behaviors of reactant molecules. Based on these results, the role of the promoters in regulating the selective hydrogenation activity will be discussed in detail.

2. Results and Discussion

2.1. Catalyst Characterization

2.1.1. Textural and Structural Properties of Catalysts

Figure 1 shows the XRD patterns of γ -Al₂O₃- and γ -Al₂O₃-supported Ni, NiCu, and NiZn catalysts after calcination at 550 °C for 3 h. For the Al₂O₃ sample, the typical peaks of γ -Al₂O₃ were observed at $2\theta = 37.7, 39.3, 45.9$, and 66.9° . As the standard XRD patterns of γ -Al₂O₃ (green bars in Figure 1) and NiAl₂O₄ (orange bars in Figure 1) are similar and difficult to identify, the relative intensity of the characteristic peaks was used to differentiate the two phases. The intensity of the peak located at 45.9° is clearly higher than that of the peak located at 37.7° , which is in good accordance with standard γ -Al₂O₃. After the impregnation of NiO, the intensity of the peak located at around 37° increased and exhibited almost the same intensity as the peak located at around 45° . This phenomenon is ascribed to the introduction of NiAl₂O₄ in C0, C1, and C2-2. According to the characteristic patterns of NiAl₂O₄, the intensity of the peak at 37.0° was higher than that of the peak at 45.0° , which led to an increasing intensity on samples with the impregnation of NiO. The characteristic peaks of NiO, CuO, and ZnO were not observed, indicating that the transition metals were highly dispersed on the alumina surface and strongly interacted with Al₂O₃.

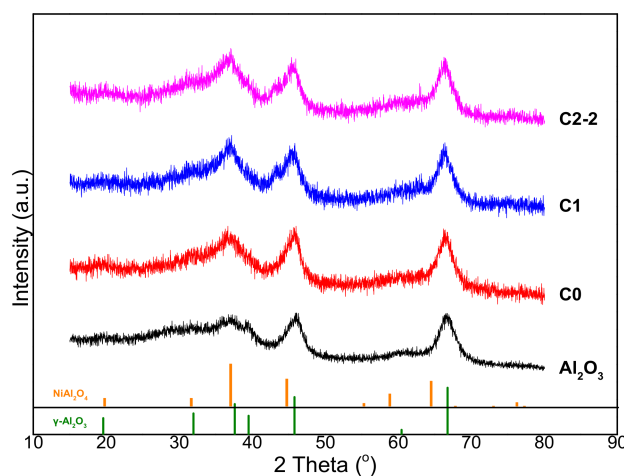


Figure 1. The XRD patterns of Al_2O_3 and M-Ni/ Al_2O_3 samples, (C0) 10Ni/ Al_2O_3 , (C1) 10Ni4Cu/ Al_2O_3 , and (C2-2) 10Ni4Zn/ Al_2O_3 .

The TEM and STEM results in Figure 2 show that the metal oxides were not uniformly dispersed on the Al_2O_3 surface. The size of the metal oxides particles ranged from 5 nm to about 15 nm. To further investigate the effect of CuO and ZnO on the Ni/ Al_2O_3 catalyst, HRTEM images (Figure 3) of NiCu/ Al_2O_3 and NiZn/ Al_2O_3 were taken. We found that CuO and NiO particles were detected and separately loaded on the Al_2O_3 surface for NiCu/ Al_2O_3 , and both the NiO and CuO particles were anchored on Al_2O_3 . In addition, although the NiO and CuO were located nearby, NiCu alloy was not observed. However, on NiZn/ Al_2O_3 , we found that some NiO and ZnO particles were closely joined together, which directly shows the interaction between ZnO and NiO. When the NiO disperses on ZnO/ Al_2O_3 surface, the interaction between NiO and Al_2O_3 may decrease accordingly.

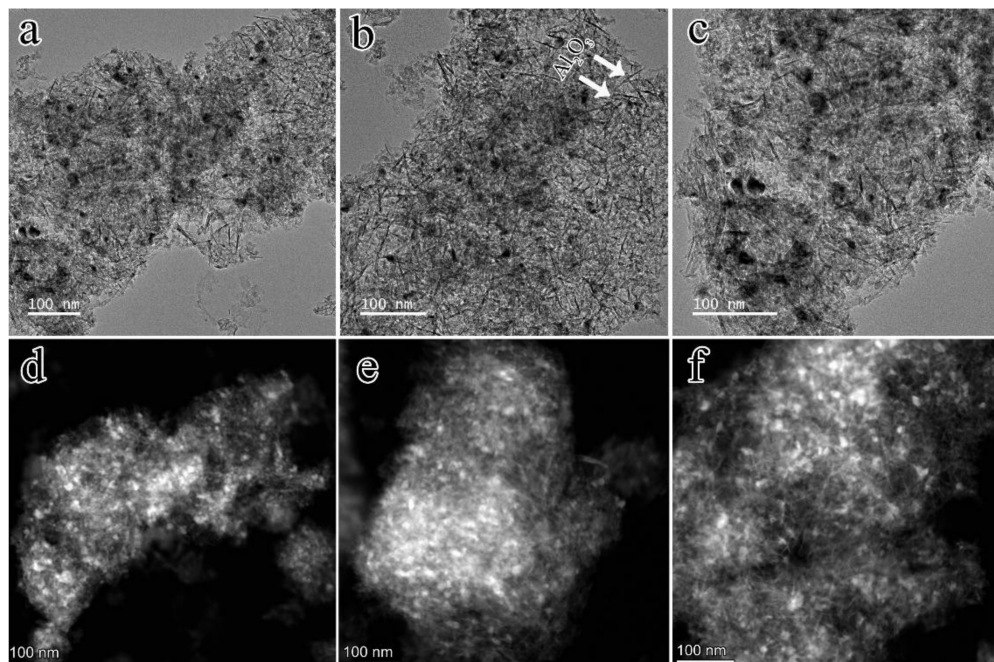


Figure 2. TEM and STEM images of (a,d) 10Ni/ Al_2O_3 , (b,e) 10Ni4Cu/ Al_2O_3 , and (c,f) 10Ni4Zn/ Al_2O_3 after calcination.

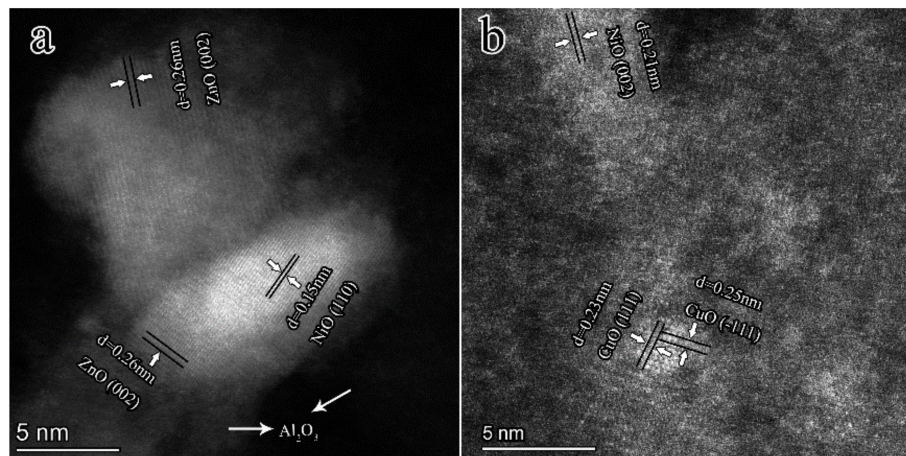


Figure 3. HRTEM images of (a) 10Ni4Zn/Al₂O₃ and (b) 10Ni4Cu/Al₂O₃ after calcination.

2.1.2. The Reducibility of Catalysts

Figure 4a shows the H₂-TPR profiles for the Ni/Al₂O₃, NiCu/Al₂O₃, and NiZn/Al₂O₃ samples. We observed that the reduction peaks of NiO_x in Ni/Al₂O₃ were in the wide temperature range of 550–800 °C and a reduction of NiO crystals appearing at 200–300 °C was not observed. The results further indicate the strong interaction between NiO_x species and the alumina support, and the Ni species in the form of Ni-Al spinel structure were more difficult to reduce than the NiO crystal [26–28].

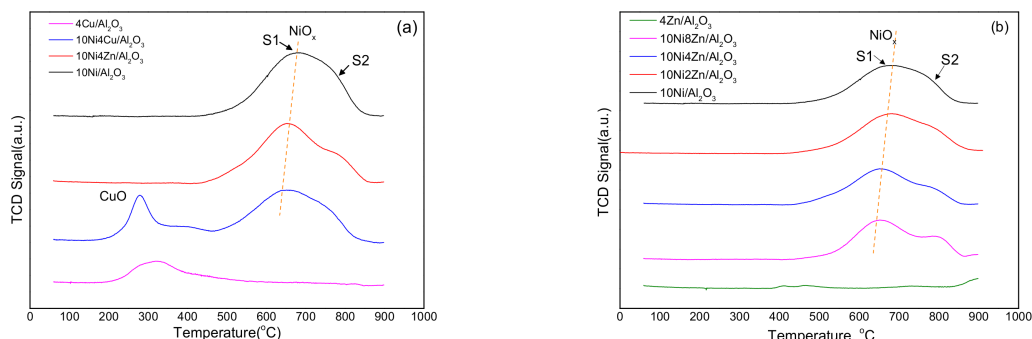


Figure 4. The H₂-TPR profiles of (a) 10Ni/Al₂O₃, 10Ni4Zn/Al₂O₃, 10Ni4Cu/Al₂O₃, Cu/Al₂O₃ and (b) 10Ni/Al₂O₃, 10Ni2Zn/Al₂O₃, 10Ni4Zn/Al₂O₃, 10Ni8Zn/Al₂O₃, 4Zn/Al₂O₃.

For the NiCu/Al₂O₃ sample, the reduction peak of CuO emerged at approximately 250 °C, which is consistent with Cu/Al₂O₃, indicating a similar state of CuO for Cu/Al₂O₃ and NiCu/Al₂O₃. The peak temperatures of NiO_x shifted from 676 °C for Ni/Al₂O₃ to 643 °C for NiCu/Al₂O₃. This shift indicates that the doping of CuO in Ni/Al₂O₃ can efficiently accelerate the reduction of NiO_x. The result can be ascribed to the spillover of H atoms, which facilitates the reduction of NiO_x. The pre-reduced Cu promotes the dissociation of absorbed H₂ to form active H species and react with the surface NiO_x through surface transport [29,30]. For the NiZn/Al₂O₃ sample, the reduction peak of NiO_x split into two peaks, located at 650 and 770 °C, separately. This indicates that the NiO_x species may exist in different forms.

Based on the HRTEM results, it is reasonable to deduce that parts of the NiO_x species can interact with ZnO and, hence, more weakly interact with Al₂O₃. These NiO_x species are marked as NiO_x(S1). The other NiO_x species interacting strongly with Al₂O₃ are marked as S2 sites. According to the different reduction temperatures in H₂-TPR, the S1 sites were more easily reduced compared with the S2 sites. To confirm this assumption, we further investigated the H₂-TPR of the samples with different

Ni/Zn ratios, and the results are given in Figure 4b. This clearly shows that the peak temperature of the S1 site decreased with the ZnO content and the relative area of the lower temperature peak increased with the ZnO content, which indicates the formation of more S1 sites on the NiZn/Al₂O₃ catalysts.

2.1.3. XPS Analysis

The chemical states of Ni on catalysts after calcination at 550 °C in the air were investigated using XPS. The samples after calcination were further reduced in 100% H₂ at 450 °C for 2 h. The reduced samples were also tested by XPS to study the change of the Ni chemical states. The Ni 2p XPS results of Ni/Al₂O₃, NiCu/Al₂O₃, and NiZn/Al₂O₃ after calcination are shown in Figure 5. After spectral deconvolution, two groups of peaks were found for Ni/Al₂O₃ with binding energies (BEs) at 875.3, 873.7, 857.9, and 856.3 eV, which are all characteristic peaks of Ni(II). This phenomenon indicates that Ni species mainly existed as Ni(II) on Ni/Al₂O₃ with two different forms. Binding energies at 873.7 and 856.3 eV were assigned to Ni(II) 2p_{1/2} and Ni(II) 2p_{3/2} of NiO_x. The two peaks located at 875.3 and 857.9 eV were indexed to Ni(II) 2p_{1/2} and Ni(II) 2p_{3/2} of NiAl₂O₄ [31,32].

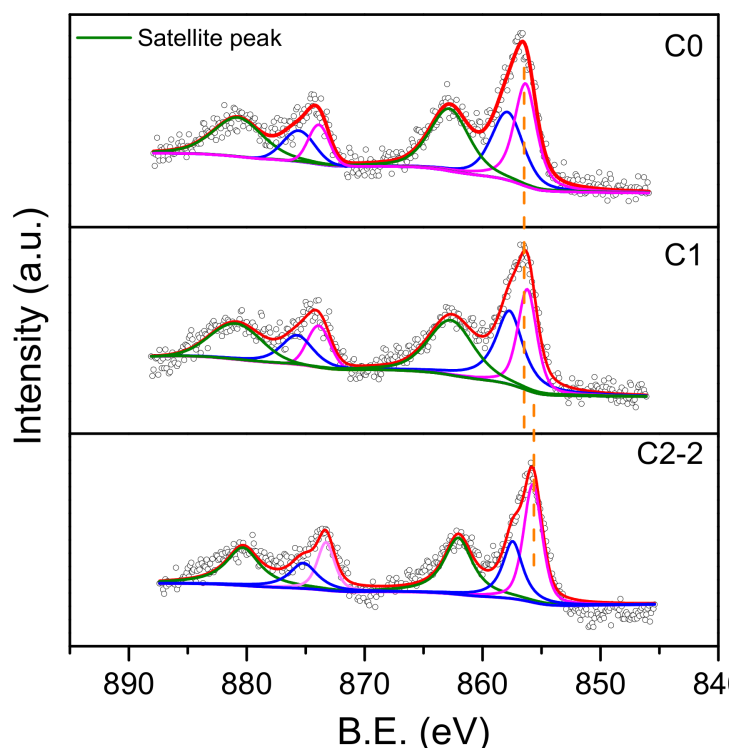


Figure 5. Ni 2p XPS spectra of the samples after calcination. (C0) 10Ni/Al₂O₃, (C1) 10Ni4Cu/Al₂O₃, and (C2-2) 10Ni4Zn/Al₂O₃.

Satellite peaks around 880.7 and 863.3 eV were observed, which are the characteristic peaks of Ni(II). The Ni 2p XPS spectrum of NiCu/Al₂O₃ is similar to that of Ni/Al₂O₃, which exists with two groups of peaks located at 875.2, 873.6, 857.8, and 856.2 eV. The binding energies of Ni(II) on NiCu/Al₂O₃ exhibited no evident difference with Ni/Al₂O₃, indicating that the CuO species have no obvious electron effects with NiO_x species. Combined with the H₂-TPR results above, this further proved that the doping of CuO mainly influences NiO_x by H spillover rather than a formation of alloy. Binding energies at 874.9, 873.1, 857.5, and 855.7 eV were ascribed to Ni(II) on NiZn/Al₂O₃. Comparing with Ni/Al₂O₃, the characteristic peaks of Ni(II) from NiAl₂O₄ on NiZn/Al₂O₃ were shifted to lower BEs (from 856.3 to 855.7 eV, and from 873.7 to 873.1 eV), and the relative peak area at 855.7 eV

also became larger. This result further confirms that the introduction of Zn species can weaken the interaction between Ni and Al_2O_3 by forming $\text{NiO}_x(\text{S}1)$ species.

To further investigate the effect of doping ZnO on the chemical states of Ni^{2+} , the XPS spectra of $\text{NiZn}/\text{Al}_2\text{O}_3$ with different ZnO contents are also shown in Figure 6. With the increasing amount of ZnO, the relative peak area of the lower binding energy increased while the peak of the higher binding energy decreased, which indicates the increase of weaker interaction $\text{NiO}_x(\text{S}1)$ species. In addition, the lower binding energy peak shifted slightly to a lower energy direction with the increase of ZnO, which illustrates that the d electrons may shift from ZnO to the NiO_x . The Ni species clearly obtain more electrons from Zn species with the increase of Zn content, which will weaken the interaction between NiO_x and molecules with Π electrons [33].

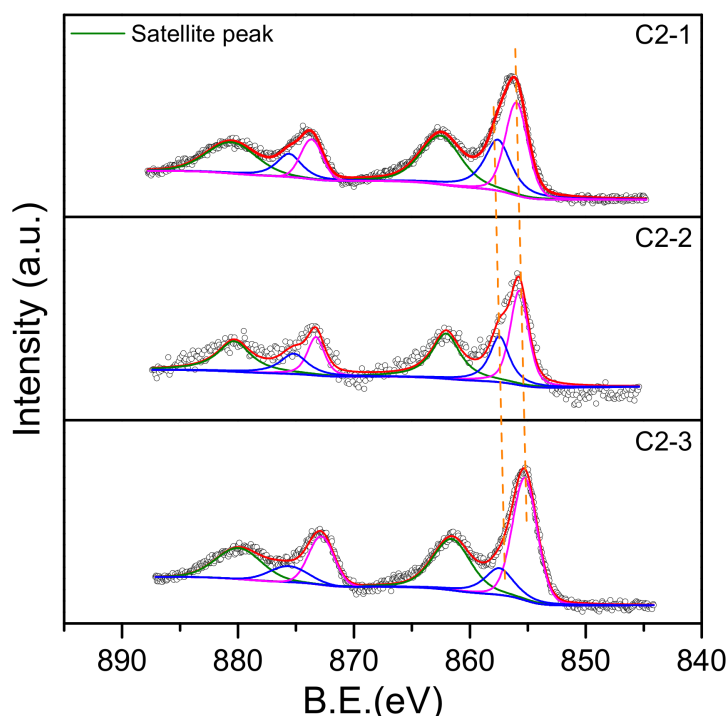


Figure 6. XPS spectra of $\text{NiZn}/\text{Al}_2\text{O}_3$ with different Ni/Zn ratios after calcination. (C2-1) $10\text{Ni}2\text{Zn}/\text{Al}_2\text{O}_3$, (C2-2) $10\text{Ni}4\text{Zn}/\text{Al}_2\text{O}_3$, and (C2-3) $10\text{Ni}8\text{Zn}/\text{Al}_2\text{O}_3$.

The XPS results of Ni supported catalysts after H_2 reduction (Figure 7) show that the spectra of Ni 2p were shifted to lower BEs at around 853, 855, 870, and 872 eV. The results show that parts of NiO and NiAl_2O_4 were reduced into low valency under 450°C . The peaks located at 853 and 870 eV are ascribed to the partly reduced NiO , denoted as $\text{Ni}^{\delta 1+}$ species, and the peaks located at 855 and 872 eV are assigned to the partly reduced NiAl_2O_4 , denoted as $\text{Ni}^{\delta 2+}$ species ($\delta 1+ < \delta 2+ < 2$). However, the ratio of $\text{Ni}^{\delta 1+}/\text{Ni}^{\delta 2+}$ is varied among the catalysts. The $\text{NiCu}/\text{Al}_2\text{O}_3$ showed the highest ratio of $\text{Ni}^{\delta 1+}$ followed by $\text{NiZn}/\text{Al}_2\text{O}_3$ and $\text{Ni}/\text{Al}_2\text{O}_3$. As discussed before, the doping of Cu can accelerate the reduction of Ni^{2+} by H spillover and the Ni^{2+} in the form of $\text{NiO}_x(\text{S}1)$ tended to be easier to reduce compared with the NiAl_2O_4 in $\text{Ni}/\text{Al}_2\text{O}_3$. We observed that Ni 2p of $\text{NiZn}/\text{Al}_2\text{O}_3$ was slightly shifted to a lower binding energy, which also indicates an electron transfer from ZnO to $\text{Ni}^{\delta+}$.

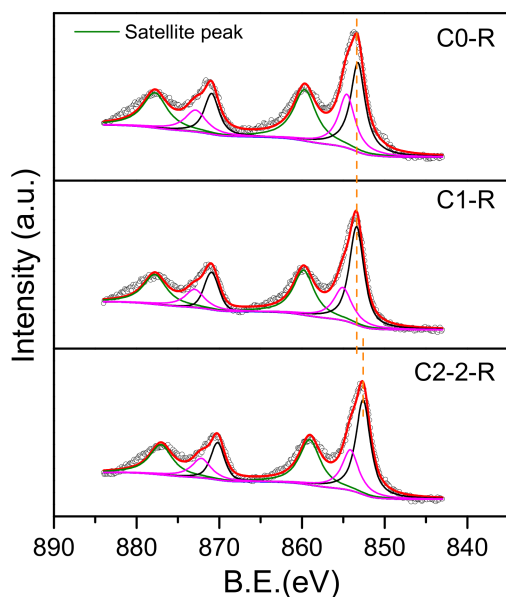


Figure 7. XPS patterns of the samples after H_2 reduction. (C0-R) $10\text{Ni}/\text{Al}_2\text{O}_3$, (C1-R) $10\text{Ni}4\text{Cu}/\text{Al}_2\text{O}_3$, and (C2-2-R) $10\text{Ni}4\text{Zn}/\text{Al}_2\text{O}_3$.

2.2. Catalytic Performance

Table 1 presents the catalytic performance of the samples. We found that a naphthalene conversion of 79.6% was achieved over a $\text{Ni}/\text{Al}_2\text{O}_3$ catalyst. The $\text{NiZn}/\text{Al}_2\text{O}_3$ and $\text{NiCu}/\text{Al}_2\text{O}_3$ catalysts showed a higher hydrogenation activity with naphthalene conversions of 86.1% and 84.9%, respectively. However, the selectivity for tetraline of $\text{NiCu}/\text{Al}_2\text{O}_3$ was 58.3%, which is much lower than that of $\text{Ni}/\text{Al}_2\text{O}_3$ (72.6%) and $\text{NiZn}/\text{Al}_2\text{O}_3$ (82.0%). As demonstrated in part 3.1, the addition of Cu in $\text{NiCu}/\text{Al}_2\text{O}_3$ can promote the reduction of NiO_x species through H spillover. Hence, $\text{NiCu}/\text{Al}_2\text{O}_3$ could form more active $\text{Ni}^{\delta+}$ ($0 \leq \delta \leq 1$) species in an H_2 atmosphere, which can enhance the hydrogenation activity of the catalysts.

Table 1. The catalytic performance of all samples.

Catalyst	Conversion (wt.%)	Selectivity (wt.%)	Yield (wt.%)
$10\text{Ni}/\text{Al}_2\text{O}_3$	79.6	72.6	57.8
$10\text{Ni}4\text{Cu}/\text{Al}_2\text{O}_3$	84.9	58.3	49.5
$10\text{Ni}2\text{Zn}/\text{Al}_2\text{O}_3$	86.7	75.4	65.4
$10\text{Ni}4\text{Zn}/\text{Al}_2\text{O}_3$	86.1	82.0	70.6
$10\text{Ni}8\text{Zn}/\text{Al}_2\text{O}_3$	84.5	87.4	73.8

In addition, due to the strong electron affinity of $\text{Ni}^{\delta+}$ ($0 \leq \delta \leq 1$) species, the aromatic ring is strongly adsorbed, which results in an excessive hydrogenation of tetraline into decalin. On the other hand, as the NiO_x species can be easier to reduce in a $\text{NiZn}/\text{Al}_2\text{O}_3$ catalyst compared with $\text{Ni}/\text{Al}_2\text{O}_3$, more $\text{Ni}^{\delta+}$ species with low valence states can be formed in an H_2 atmosphere, which leads to improved hydrogenation activity. However, as Zn^{2+} species tend to provide electrons to $\text{Ni}^{\delta+}$, the $\text{NiZn}/\text{Al}_2\text{O}_3$ catalyst had a lower adsorption ability for tetraline than $\text{Ni}/\text{Al}_2\text{O}_3$ and $\text{NiCu}/\text{Al}_2\text{O}_3$. The excessive hydrogenation of tetraline was inhibited in $\text{NiZn}/\text{Al}_2\text{O}_3$ and resulted in improved tetraline selectivity.

Table 1 also shows the catalytic performance of $\text{NiZn}/\text{Al}_2\text{O}_3$ catalysts with different Ni/Zn ratios. The naphthalene conversion decreased slightly from 86.7% to 84.5% while the tetraline selectivity increased from 75.4% to 87.4% when the Ni/Zn ratio decreased from 5 to 1.25. The significant improvement in selectivity was mainly determined by the naphthalene and tetraline adsorption ability. As more S1 centers are formed in the catalysts with the Zn content, the adsorption ability of $\text{Ni}^{\delta+}$ for

naphthalene and tetraline become weaker due to the electron transfer, which results in the slightly lower naphthalene conversion but higher tetraline selectivity.

2.3. Computational Results

2.3.1. Gas Phase Clusters

In order to reveal the structure activity relationship of the catalysts, we performed density functional theory (DFT) calculations to investigate the adsorption of the reactants on the model catalyst surface. Figure 8 gives the structures and energies of the metal cluster and the adsorption of H₂ on the metal clusters. The results show that the Ni₄ cluster had the largest binding energy (−1168 kJ/mol), followed by Ni₂Cu₂, Ni₂Zn₂, Cu₄, and Zn₄, revealing the strongest binding of Ni, and the weakest binding of Zn₄. In addition, the structures of Ni₄ and Zn₄ were regular tetrahedron, vs. the planar rhombic of Ni₂Cu₂, Ni₂Zn₂, and Cu₄. The Ni₂Cu₂ had the largest adsorption energy for H₂ (−711 kJ/mol), followed by Cu₄ (−627 kJ/mol), Ni₄ (−145 kJ/mol), and Ni₂Zn₂ (−108 kJ/mol). This indicates that the Cu promoted the H₂ adsorption on the Ni cluster, vs. the Zn, which inhibited the adsorption of H₂ on the Ni cluster.

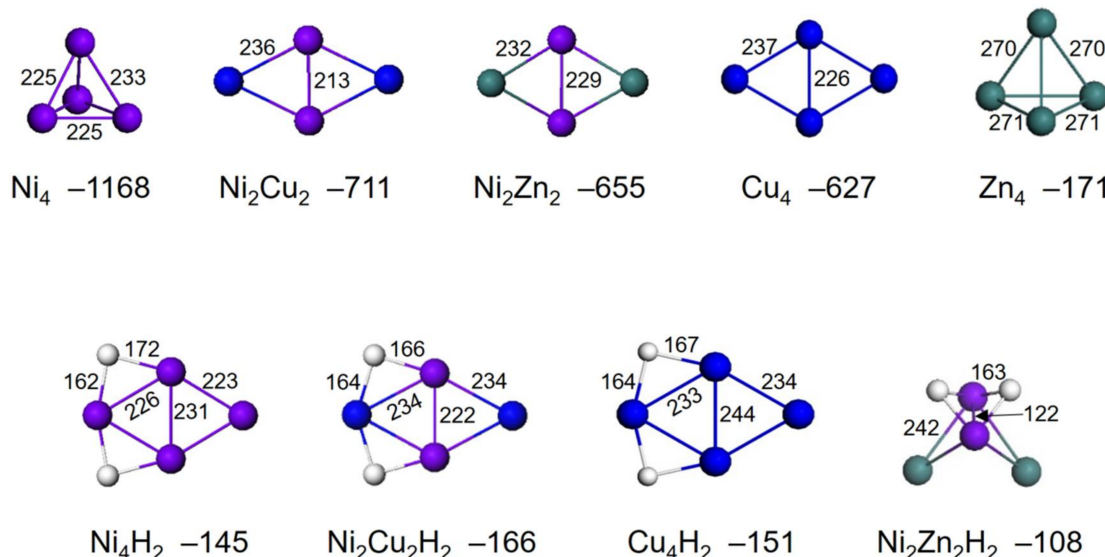


Figure 8. The structures, bond distances (pm), binding energies (kJ/mol), and adsorption energies (kJ/mol) for H₂ on metal clusters. H, Ni, Cu, and Zn atoms are shown in white, violet, blue, and olive green, respectively.

2.3.2. The Adsorption of Metal Clusters on the Alumina Surface and Molecules on the Model Catalysts

Figure 9 shows all the possible models of metal clusters on the alumina surface, as well as the adsorption of H₂, naphthalene, and tetralin on the model catalysts. Accordingly, the Ni₄ maintained its gas phase tetrahedron structure, vs. the 'Y' shape structure of Cu₄. However, the Zn₄ exists as the form of two isolated Zn₂ dimer with an adsorption energy of −235 kJ/mol, indicating the weak interaction of Zn with the alumina surface. The adsorption energies of the metal clusters on the alumina surface follow the order: Zn₄ < Cu₄ < Ni₂Zn₂ < Ni₂Cu₂ < Ni₄. The adsorption of H₂ on the supported model catalysts follow the order: Zn₄ < Ni₂Zn₂ < Ni₂Cu₂ < Ni₄ < Cu₄, indicating the Cu₄ cluster had the highest activity for H₂ activation and was able to induce H₂ dissociative adsorption.

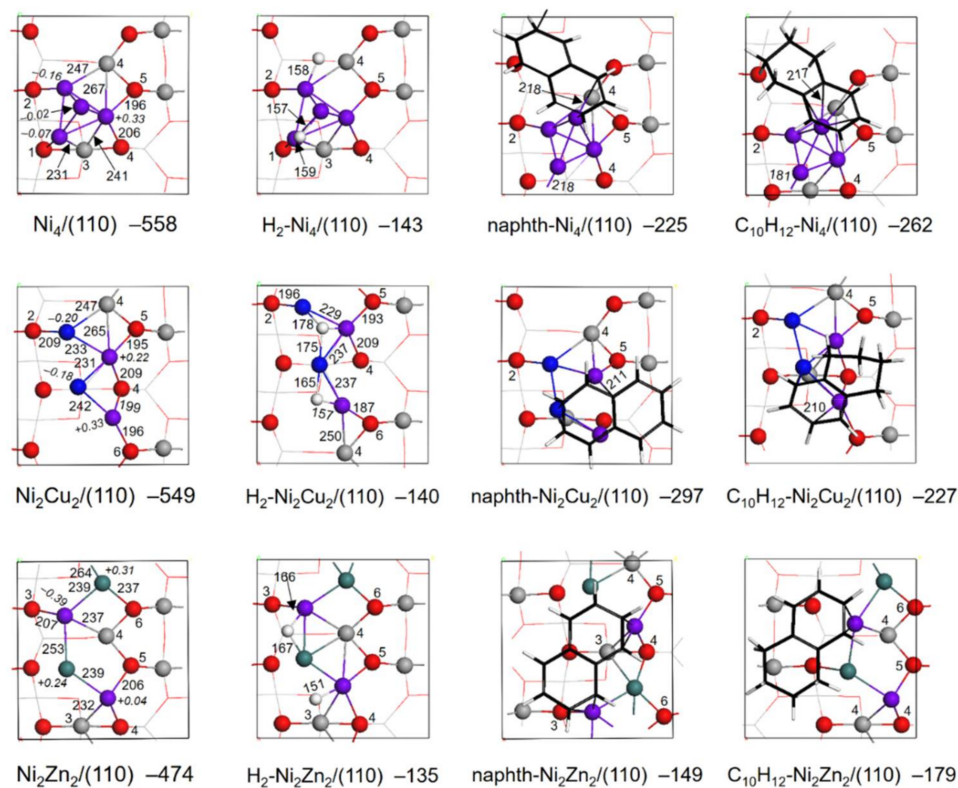


Figure 9. The structures for the adsorption of metal clusters on the alumina surface and the adsorption of H_2 , naphthalene, and tetraline on the model catalysts. The adsorption energy (kJ/mol), bond distance (pm), and Bader charge (e) are given. H, O, Al, Ni, Cu, and Zn atoms are shown in white, red, grey, violet, blue, and olive green, respectively.

Theoretically, the alumina supported Ni_2Cu_2 had the highest activity for naphthalene adsorption with adsorption energy of -297 kJ/mol , vs. -225 , -167 , -149 , and -95 kJ/mol on the alumina supported Ni_4 , Cu_4 , Ni_2Zn_2 , and Zn_4 clusters, respectively. The calculated adsorption energy for tetraline on the alumina supported Ni_4 model catalyst was -262 kJ/mol , followed by -227 , -201 , -179 , and -132 kJ/mol on the alumina supported Ni_2Cu_2 , Cu_4 , Ni_2Zn_2 , and Zn_4 clusters, respectively. From the experimental results, NiCu clusters may actually not exist due to the high temperature calcinations, and only Cu and NiO_x clusters should be considered in the $\text{NiCu}/\text{Al}_2\text{O}_3$ catalyst.

Although the Ni cluster showed higher adsorption ability for naphthalene and H_2 than the NiZn cluster in theory, the conversion of $\text{Ni}/\text{Al}_2\text{O}_3$ was lower than that of $\text{NiZn}/\text{Al}_2\text{O}_3$; this is mainly ascribed to the lower quantity of the reduced NiO_x cluster under the H_2 atmosphere in $\text{Ni}/\text{Al}_2\text{O}_3$ compared with $\text{NiZn}/\text{Al}_2\text{O}_3$. In addition, the DFT results presented that the NiZn clusters in the $\text{NiZn}/\text{Al}_2\text{O}_3$ catalyst had a lower tetraline adsorption energy compared with Ni and Cu, which is a benefit for the tetraline desorption during the reaction and, hence, increased the tetraline selectivity for the $\text{NiZn}/\text{Al}_2\text{O}_3$ catalyst.

The Bader charge analysis showed that the ZnNiO_x alloy did present an electron transfer effect (confirming the XPS and $\text{H}_2\text{-TPR}$ results), which led to a reasonable adsorption of naphthalene and tetraline on the catalysts [34]. The optimization of the product adsorption is the primary cause of the improved tetralin selectivity on the $\text{NiZn}/\text{Al}_2\text{O}_3$ catalyst.

3. Conclusions

In summary, Cu and Zn were introduced into $\text{Ni}/\text{Al}_2\text{O}_3$ catalysts, and the selective hydrogenation of naphthalene to tetraline was investigated thoroughly over these catalysts. On one hand, both Cu and Zn efficiently promoted the hydrogenation activity of $\text{Ni}/\text{Al}_2\text{O}_3$. On the other hand, Cu promoters

decreased the tetraline selectivity; however, Zn modification improved the selectivity. In the NiCu/Al₂O₃ catalysts, NiCuO_x alloy was not formed, and the electrical transfer between Ni and Cu was not obvious. However, the Cu promoter induced H spillover and accelerated the reduction of NiO_x species, as well as naphthalene hydrogenation, which promoted the hydrogenation activity, however, with a decrease in the tetraline selectivity.

We found that the doping of ZnO weakened the interaction between NiO_x and Al₂O₃ and promoted the formation of NiO_x(S1) species in NiZn/Al₂O₃. The NiO_x(S1) species have a good reducibility, resulting in an improvement of the naphthalene hydrogenation activity. The greatly increased tetraline selectivity is ascribed to the optimized adsorption of the tetraline product on the Ni^{δ+} active sites, which resulted from the electron transferring between ZnO and NiO_x. This work elucidated the mechanism of the structure regulation of NiM/Al₂O₃(M = Cu, Zn) for selective hydrogenation of naphthalene, and this opens up a new opportunity to develop efficient industry catalysts for heavy aromatics conversion.

4. Materials and Methods

4.1. Experimental Details

4.1.1. Reagents

Tridecane, naphthalene, Ni(NO₃)₂·6H₂O, Cu(NO₃)₂·3H₂O, and Zn(NO₃)₂·6H₂O were of analytical reagent grade and were purchased from Sinopharm Chemical Reagent Co., Ltd. γ-Al₂O₃ (*d* = 2 mm) was purchased from ZiBo HengQi Powder New Materials Co., Ltd (Zibo City, Shandong Province, China). All chemicals were used without further purification.

4.1.2. Catalysts Preparation

We calcined 20 g of γ-Al₂O₃ at 400 °C for 4 h and cooled it down to room temperature in a drier, which was used as a support. Ni(NO₃)₂·6H₂O (9.90 g) was dissolved in purified water (8 mL) to obtain the impregnating solutions. Then, the γ-Al₂O₃ support was mixed with the above nitrate solution by an incipient impregnation, and the C0 catalyst was obtained after drying at 120 °C for 12 h and then calcining at 550 °C for 3 h. The designed mass loading of Ni atoms was of 10 wt.%, and the C0 catalyst was defined as 10Ni/Al₂O₃ in Table 2. Similarly, the C1 catalyst was produced by the incipient impregnation of the γ-Al₂O₃ support with Ni(NO₃)₂·6H₂O (9.90 g) and Cu(NO₃)₂·3H₂O (3.39 g) mixing solution. The designed mass loading of Ni and Cu atoms were 10 wt.% and 4 wt.%, respectively, which was named as 10Ni4Cu/Al₂O₃. In this manner, the C2-1, C2-2, and C2-3 catalysts were prepared with the same procedure as the C1 catalyst with the designed Ni mass loading of 10 wt.%, and the designed Zn mass loadings were 2 wt.%, 4 wt.%, and 8 wt.%, respectively. The actual mass loading of the metal atom in the catalysts was analyzed using inductively coupled plasma-atomic emission spectroscopy (ICP-AES), and the labels and corresponding compositions of the catalysts are listed in Table 2.

Table 2. The catalyst compositions of NiM/Al₂O₃.

Catalyst	Compositions	Content of Ni (wt.%) ^a	Content of M (wt.%) ^a	BET Surface Area (m ² /g) ^b	Pore Volume (cm ³ /g) ^c
C0	10Ni/Al ₂ O ₃	9.3	/	230	0.61
C1	10Ni4Cu/Al ₂ O ₃	9.5	4.1	226	0.55
C2-1	10Ni2Zn/Al ₂ O ₃	9.3	1.9	225	0.56
C2-2	10Ni4Zn/Al ₂ O ₃	9.7	3.9	221	0.54
C2-3	10Ni8Zn/Al ₂ O ₃	9.7	7.8	215	0.53

^a tested by inductively coupled plasma-atomic emission spectroscopy (ICP-AES), ^b surface area calculated by Brunauer-Emmet-Teller (BET) equation, ^c sum of the microporous and mesoporous volumes.

4.1.3. Catalysts Characterization

The powder X-ray diffraction (XRD) patterns were performed to characterize the crystal phase of the catalysts with the D/Max2550 VB/PC diffract meter instrument (Rigaku Corporation, Japan) operating at 40 kV and 40 mA with CuK α radiation ($\lambda = 0.154056$ nm), and the diffraction data (2θ) was collected between 10–90° with a scanning rate of 8°/min. The metal mass loading was determined by an inductively coupled plasma-atomic emission spectroscopy (ICP-AES, Thermo Fisher Scientific Inc., Waltham, MA, USA). The H₂ temperature-programmed reduction (H₂-TPR) was operated on an automated chemisorption analyzer from Micromeritics Instrument Corporation (AutoChem 2920 II, Norcross, GA, USA) with a thermal conductivity detector (TCD). In detail, 30 mg of catalysts were used and pretreated at 400 °C for 1 h with a heating rate of 10 °C/min in an Ar flow (30 mL·min⁻¹) to remove the absorbed impurities. After being cooled to room temperature under Ar, the catalyst was flushed with 10% H₂/Ar at 30 mL·min⁻¹ instead of pure Ar, and the TPR profiles were obtained with a temperature ramp of 10 °C/min.

X-ray photoelectron spectra (XPS) were acquired on an ESCALAB250 X-ray photoelectron spectroscopy of Thermo Fisher Scientific Inc., (Massachusetts, Waltham, MA, USA) using C 1s (284.6 eV) as a reference. The reduction of the catalysts for XPS test in Figure 8 was conducted in a fixed-bed reactor with pure H₂, and the detailed conditions are given in Chapter 4.1.4. In order to avoid air exposure, the reaction tube was displaced with high purity nitrogen after the reduction. Then, the two shut-off valves on the top and bottom of the reaction tube were closed with pressurized nitrogen filling the interior. The sealed reaction tube was removed and then transferred into the nitrogen filled glove box. The XPS sample preparation was finished in the glove box and then transferred into the XPS equipment to complete the following test. The obtained data were analyzed with the XPSpeak41 software. High-resolution transmission electron microscopy (HRTEM) and scanning transmission electron microscopy were performed using a Tecnai 20 S-TWIN at 200 kV (FEI Company, Hillsboro, OR, USA).

4.1.4. Catalysts Evaluation

Tridecane and naphthalene were mixed to prepare the feed for the reaction with 8.5 wt.% naphthalene. The reaction was performed with a fixed-bed reactor, loaded with 5 g of catalysts. All catalysts were online reduced in H₂ flowing at 450 °C for 2 h before reaction, and then the reactions were carried out with the weight hourly space velocity (WHSV) at 3.0 h⁻¹, the molar ratio of H₂/hydrocarbon at 3.0, the pressure at 3.0 MPa, and the reaction temperature at 375 °C. The products were analyzed with Agilent gas chromatography 7890B with a flame ionization detector (FID) detector and HP-FFAP column (Agilent, Santa Clara, CA, USA). The conversion of naphthalene (X) and the selectivity (S) and yields (Y) for tetralin were calculated as follows:

$$X = \frac{n_0 - n_1}{n_0} \times 100\% \quad (1)$$

$$S = \frac{n_2}{n_0 - n_1} \times 100\% \quad (2)$$

$$Y = X \times S \times 100\% \quad (3)$$

in which n_0 and n_1 represent the weight content of naphthalene (wt.%) in the feed and liquid product, and n_2 represents the weight content of tetralin (wt.%) in the liquid products.

4.2. Computational Details

The non-spinel γ -Al₂O₃ model proposed by Digne et al. was used to describe the γ -Al₂O₃ surface, in which more than 70% of the γ -Al₂O₃ (110) surface was exposed under the real catalytic conditions [35,36]. The p (1 × 1) super cell model with a dimension of 67.86 Å² was applied. Sixteen Al₂O₃ unit cells were distributed in eight atomic layers, with a 15 Å vacuum layer separating

the slabs in the z direction of the surface. The bottom four layers were frozen in their bulk positions, and the top four layers together with the adsorbed species were allowed to fully relax.

Figure 10 shows the side and the top views of the $\gamma\text{-Al}_2\text{O}_3$ (110) surface with the topmost atoms labeled with numbers. On the clean surface, tri-coordinated aluminum (Al_{3c}), tetra-coordinated aluminum (Al_{4c}), di-coordinated oxygen (O_{2c}), and tri-coordinated oxygen (O_{3c}) atoms were exposed, and were unsaturated in coordination.

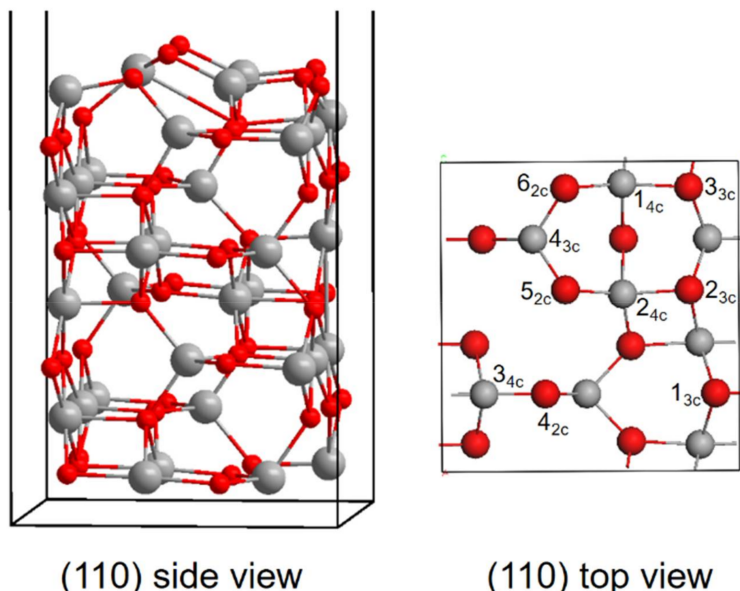


Figure 10. The structures for the $\gamma\text{-Al}_2\text{O}_3$ (110) surface. O and Al atoms are shown in red and grey, respectively. The exposed top layer atoms are indexed with numbers, and the coordination numbers are shown in subscripts.

All computational works were calculated with the PBE-D method with plane wave basis setting as in the VASP code [37,38]. The D3 method was performed to calculate the dispersive interactions for the optimized adsorption structures. The exchange and correlation energies were described by the generalized gradient approximation (GGA) formulation with the PBE functional [39]. The Kohn-Sham one-electron states were extended in accordance with plane-wave basis sets with the cut off energy of 350 eV. The projector augmented wave (PAW) method was applied to describe the electron-ion interactions [40,41]. The Brillouin zone was generated by the Monkhorst–Pack algorithm, and sampled with $5 \times 5 \times 5$ and $3 \times 3 \times 1$ k -point meshes used for the unit cell and surface slabs, respectively. The gas molecules were calculated in a $15 \times 15 \times 15 \text{ \AA}^3$ cubic lattice. The convergence criteria were set at 1.0×10^{-5} eV for the SCF energy, 1×10^{-4} eV and $0.03 \text{ eV}/\text{\AA}$ for the total energy and the atomic forces, respectively.

The adsorption energies (E_{ads}) for the adsorption of molecules in the surface were calculated as:

$$E_{ads} = E(\text{M/slab}) - [E(\text{M}) + E(\text{slab})] \quad (4)$$

where $E(\text{M/slab})$, $E(\text{M})$, and $E(\text{slab})$ were the total energies of the spinel surface slab with the adsorbed molecule, the isolated gas phase molecule, and the surface, respectively.

The binding energies of the gas phase cluster were calculated as:

$$E_{bind}(\text{M}_n) = E(\text{M}_n) - nE(\text{M}). \quad (5)$$

The adsorption energy for single H_2 molecule on the metal cluster were calculated as:

$$E_{ads}(\text{MnH}_2) = E(\text{MnH}_2) - E(\text{Mn}) - E(\text{H}_2), \quad (6)$$

where $E(M_n)$, $E(M_nH_2)$, $E(M)$, and $E(H_2)$ were the energies of the isolated gas phase M_n , M_nH_2 cluster, single M atom and H_2 molecule, respectively.

Author Contributions: Conceptualization, J.L.; methodology, G.F.; software, L.S.; validation, D.K. and C.S.; investigation, J.L.; writing—original draft preparation, J.L. and L.S.; writing—review and editing, Z.S.; supervision, C.S. All authors have read and agreed to the published version of the manuscript.

Funding: This research was funded by the National Natural Science Foundation of China, Grant Number 21763018 and 21875096.

Acknowledgments: This work has been supported by the National Natural Science Foundation of China (Grants Nos. 21763018 and 21875096), and the Natural Science Foundation of Jiangxi Province, China (Grants No. 20181BAB203016, 20181BCD40004).

Conflicts of Interest: The authors declare no conflict of interest.

References

1. Junlin, Z.; Xuan, X.; Xiaolan, Q.; Dejin, K. Low quality heavy aromatic resources and relevant processing technology to produce fundamental petrochemicals. *Chem. Ind. Eng. Prog.* **2017**, *36*, 3665–3673.
2. Chareonpanich, M.; Boonfueng, T.; Limtrakul, J. Production of aromatic hydrocarbons from Mae-Moh lignite. *Fuel Process. Technol.* **2002**, *79*, 171–179. [[CrossRef](#)]
3. Chareonpanich, M.; Zhang, Z.-G.; Nishijima, A.; Tomita, A. Effect of catalysts on yields of monocyclic aromatic hydrocarbons in hydrocracking of coal volatile matter. *Fuel* **1995**, *74*, 1636–1640. [[CrossRef](#)]
4. Shin, J.; Oh, Y.; Choi, Y.; Lee, J.; Lee, J.K. Design of selective hydrocracking catalysts for BTX production from diesel-boiling-range polycyclic aromatic hydrocarbons. *Appl. Catal. A* **2017**, *547*, 12–21. [[CrossRef](#)]
5. Park, J.-I.; Lee, J.-K.; Miyawaki, J.; Kim, Y.-K.; Yoon, S.-H.; Mochida, I. Hydro-conversion of 1-methyl naphthalene into (alkyl)benzenes over alumina-coated USY zeolite-supported NiMoS catalysts. *Fuel* **2011**, *90*, 182–189. [[CrossRef](#)]
6. Upare, D.P.; Park, S.; Kim, M.S.; Kim, J.; Lee, D.; Lee, J.; Chang, H.; Choi, W.; Choi, S.; Jeon, Y.P.; et al. Cobalt promoted Mo/beta zeolite for selective hydrocracking of tetralin and pyrolysis fuel oil into monocyclic aromatic hydrocarbons. *J. Ind. Eng. Chem.* **2016**, *35*, 99–107. [[CrossRef](#)]
7. Jin, N.; Wang, G.; Yao, L.; Hu, M.; Gao, J. Synergistic process for FCC light cycle oil efficient conversion to produce high-octane number gasoline. *Ind. Eng. Chem. Res.* **2016**, *55*, 5108–5115. [[CrossRef](#)]
8. Choi, Y.; Lee, J.; Shin, J.; Lee, S.; Kim, D.; Lee, J.K. Selective hydroconversion of naphthalenes into light alkyl-aromatic hydrocarbons. *Appl. Catal. A* **2015**, *492*, 140–150. [[CrossRef](#)]
9. Lee, J.; Choi, Y.; Shin, J.; Lee, J.K. Selective hydrocracking of tetralin for light aromatic hydrocarbons. *Catal. Today* **2016**, *265*, 144–153. [[CrossRef](#)]
10. Kim, Y.-S.; Yun, G.-N.; Lee, Y.-K. Novel Ni_2P /zeolite catalysts for naphthalene hydrocracking to BTX. *Catal. Commun.* **2014**, *45*, 133–138. [[CrossRef](#)]
11. Galadima, A.; Muraza, O. Ring opening of hydrocarbons for diesel and aromatics production: Design of heterogeneous catalytic systems. *Fuel* **2016**, *181*, 618–629. [[CrossRef](#)]
12. Li, Z.; Chen, X. Influence of Pt on naphthalene conversion over nickel-based catalysts. *Chin. J. Catal.* **2003**, *24*, 253–258.
13. Santikunaporn, M.; Herrera, J.E.; Jongpatiwut, S.; Resasco, D.E.; Alvarez, W.E.; Sughrue, E.L. Ring opening of decalin and tetralin on HY and Pt/HY zeolite catalysts. *J. Catal.* **2004**, *228*, 100–113. [[CrossRef](#)]
14. Corma, A.; González-Alfaro, V.; Orchillés, A.V. Decalin and tetralin as probe molecules for cracking and hydrotreating the light cycle oil. *J. Catal.* **2001**, *200*, 34–44. [[CrossRef](#)]
15. Zhao, M.; Wei, X.; Zong, Z. Preparation of a new solid acid and its catalytic performance in di (1-naphthyl) methane hydrocracking. *Chin. J. Catal.* **2016**, *37*, 1324–1330. [[CrossRef](#)]
16. McVicker, G.B.; Daage, M.; Touvelle, M.S.; Hudson, C.W.; Klein, D.P.; Baird, W.C.; Cook, B.R.; Chen, J.G.; Hantzer, S.; Vaughan, D.E.W.; et al. Selective ring opening of naphthenic molecules. *J. Catal.* **2002**, *210*, 137–148. [[CrossRef](#)]
17. Mi, X.; Yang, S.; He, G.; Luo, G.; Xu, X.; Jin, H. Effects of preparation conditions for $Ni/\gamma-Al_2O_3$ catalyst on saturated hydrogenation of naphthalene. *Pet. Technol.* **2017**, *46*(4), 414–421.
18. Zhu, H.; Zhang, Y.; Qiu, Z.; Cui, H.; Zhao, L. Effects of Reaction Conditions on Saturated Hydrogenation of Naphthalene. *Fine Chem.* **2009**, *26*(5): 512–516.

19. Chen, Z.; Chen, M.; Li, C.; Xu, Y. Effect of impregnation-hydrothermal method on the structure and performance of Ni/Al₂O₃ catalyst. *Shandong Chem. Ind.* **2018**, *47*, 24–25.
20. Mi, X.; He, G.; Guo, X.; Yang, S.; Luo, G.; Xu, X.; Jin, H. Effect of reaction conditions on the hydrogenation of naphthalene to decalin over Ni/γ-Al₂O₃ catalyst. *J. Fuel. Chem. Technol.* **2018**, *46*, 879–885.
21. Ren, J.; Tang, Z.; Guo, Y.; Wang, D. Ni-M/Al₂O₃ catalysts performance for selective hydrogenation of heavy reforming aromatics. *Chem. React. Eng. Technol.* **2016**, *32*, 211–216.
22. Park, J.-I.; Ali, S.A.; Alhooshani, K.; Azizi, N.; Miyawaki, J.; Kim, T.; Lee, Y.; Kim, H.-S.; Yoon, S.-H.; Mochida, I. Mild hydrocracking of 1-methyl naphthalene (1-MN) over alumina modified zeolite. *J. Ind. Eng. Chem.* **2013**, *19*, 627–632. [[CrossRef](#)]
23. Kirumaki, S.R.; Shpeizer, B.G.; Sagar, G.V.; Chary, K.V.R.; Clearfield, A. Hydrogenation of naphthalene over NiO/SiO₂–Al₂O₃ catalysts: Structure–activity correlation. *J. Catal.* **2006**, *242*, 319–331. [[CrossRef](#)]
24. Liu, Y.; Li, W.; Liu, C.; Cui, M. Hydrogenation of naphthalene on HY/MCM-41/γ-Al₂O₃-supported sulfided Ni-Mo-P catalyst. *Chin. J. Catal.* **2004**, *25*, 537–541.
25. Lylykangas, M.S.; Rautanen, P.A.; Krause, A.O.I. Liquid-phase hydrogenation kinetics of multicomponent aromatic mixtures on Ni/Al₂O₃. *Ind. Eng. Chem. Res.* **2002**, *41*, 5632–5639. [[CrossRef](#)]
26. Rynkowski, J.; Paryjczak, T.; Lenik, M. On the nature of oxidic nickel phases in NiO/γ-Al₂O₃ catalysts. *Appl. Catal. A* **1993**, *106*, 73–82. [[CrossRef](#)]
27. Guimon, C.; Auroux, A.; Romero, E.; Monzon, A. Acetylene hydrogenation over Ni–Si–Al mixed oxides prepared by sol–gel technique. *Appl. Catal. A* **2003**, *251*, 199–214. [[CrossRef](#)]
28. Zhang, J.; Xu, H.; Jin, X.; Ge, Q.; Li, W. Characterizations and activities of the nano-sized Ni/Al₂O₃ and Ni/La-Al₂O₃ catalysts for NH₃ decomposition. *Appl. Catal. A* **2005**, *290*, 87–96. [[CrossRef](#)]
29. Feng, G.; Ganduglia-Pirovano, M.V.; Huo, C.-F.; Sauer, J. Hydrogen spillover to copper clusters on hydroxylated γ-Al₂O₃. *J. Phys. Chem. C* **2018**, *122*, 18445–18455. [[CrossRef](#)]
30. Hierl, R.; Knözinger, H.; Urbach, H.-P. Surface properties and reduction behavior of calcined CuOAl₂O₃ and CuO-NiOAl₂O₃ catalysts. *J. Catal.* **1981**, *69*, 475–486. [[CrossRef](#)]
31. Ma, Z.; Jiang, Q.-Z.; Wang, X.; Zhang, W.-G.; Ma, Z.-F. CO₂ reforming of dimethyl ether over Ni/γ-Al₂O₃ catalyst. *Catal. Commun.* **2012**, *17*, 49–53. [[CrossRef](#)]
32. Poncelet, G.; Centeno, M.A.; Molina, R. Characterization of reduced α-alumina-supported nickel catalysts by spectroscopic and chemisorption measurements. *Appl. Catal. A* **2005**, *288*, 232–242. [[CrossRef](#)]
33. Yan-peng, L.; Da-peng, L.; Chen-guang, L. Pt-K/Al₂O₃ dehydrogenation catalyst for synthesis of o-phenyl phenol(I): Promotion effect of potassium species. *J. China U Petrol. Nat. Sci.* **2012**, *36*, 165–174.
34. Henkelman, G.; Arnaldsson, A.; Jónsson, H. A fast and robust algorithm for Bader decomposition of charge density. *Comput. Mater. Sci.* **2006**, *36*, 354–360. [[CrossRef](#)]
35. Digne, M.; Sautet, P.; Raybaud, P.; Euzen, P.; Toulhoat, H. Use of DFT to achieve a rational understanding of acid–basic properties of γ-alumina surfaces. *J. Catal.* **2012**, *226*, 54–68. [[CrossRef](#)]
36. Krokidis, X.; Raybaud, P.; Gobichon, A.E.; Rebours, B.; Euzen, P.; Toulhoat, H. Theoretical study of the dehydration process of boehmite to γ-alumina. *J. Phys. Chem. B* **2001**, *105*, 5121–5130. [[CrossRef](#)]
37. Kresse, G.; Furthmüller, J. Efficiency of ab-initio total energy calculations for metals and semiconductors using a plane-wave basis set. *Comp. Mater. Sci.* **1996**, *6*, 15–50. [[CrossRef](#)]
38. Kresse, G.; Furthmüller, J. Efficient iterative schemes for ab initio total-energy calculations using a plane-wave basis set. *Phys. Rev. B* **1996**, *54*, 11169–11186. [[CrossRef](#)] [[PubMed](#)]
39. Perdew, J.P.; Burke, K.; Ernzerhof, M. Generalized gradient approximation made simple. *Phys. Rev. Lett.* **1996**, *77*, 3865–3868. [[CrossRef](#)]
40. Blöchl, P.E.; Först, C.J.; Schimpl, J. Projector augmented wave method: Ab initio molecular dynamics with full wave functions. *Bull. Mater. Sci.* **2003**, *26*, 33–41. [[CrossRef](#)]
41. PE, B. Projector augmented-wave method. *Phys. Rev. B* **1994**, *50*, 17953–17979.

Publisher's Note: MDPI stays neutral with regard to jurisdictional claims in published maps and institutional affiliations.



© 2020 by the authors. Licensee MDPI, Basel, Switzerland. This article is an open access article distributed under the terms and conditions of the Creative Commons Attribution (CC BY) license (<http://creativecommons.org/licenses/by/4.0/>).